CHEMISTRY OF MATERIALS

ARTICLE

pubs.acs.org/cm

Graphene-Based Non-Noble-Metal Catalysts for Oxygen Reduction Reaction in Acid

Hye Ryung Byon,[†,‡,§,∥] Jin Suntivich,[‡,§] and Yang Shao-Horn*[,†,‡,§]

[†]Department of Mechanical Engineering, [‡]Department of Materials Science and Engineering, and [§]Electrochemical Energy Laboratory, Massachusetts Institute of Technology, Cambridge, Massachusetts 02139-4307, United States

Supporting Information

ABSTRACT: Non-noble-metal catalysts based on Fe−N−C moieties have shown promising oxygen reduction reaction (ORR) activity in proton exchange membrane fuel cells (PEMFCs). In this study, we report a facile method to prepare a Fe−N−C catalyst based on modified graphene (Fe−N−*r*GO) from heat treatment of a mixture of Fe salt, graphitic carbon nitride (g-C_3N_4), and chemically reduced graphene (*r*GO). The Fe−N−*r*GO catalyst was found to have pyridinic N-dominant heterocyclic N (40% atomic concentration among all N components) on the surface and have an average Fe coordination of ∼3 N ($Fe-N_{3,average}$) in bulk. Rotating disk electrode measurements revealed that Fe−N−*r*GO had high mass activity in acid and exhibited high stability at 0.5 V at 80 °C in acid over 70 h, which was correlated to low H_2O_2 production shown from rotating ring disk electrode measurements.

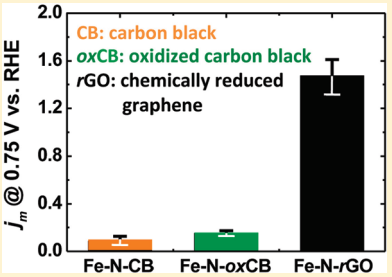

KEYWORDS: non-noble-metal catalyst, graphene, Fe−N, oxygen reduction reaction, proton exchange membrane fuel cell

INTRODUCTION

Intense research efforts have been focused on the development of non-noble-metal catalysts (NNMCs) to replace Pt for catalyzing oxygen reduction reaction (ORR), and to reduce the cost of proton exchange membrane fuel cells (PEMFCs).[1] Catalysts with Fe (or Co) coordinated to heterocyclic nitrogen (N) are among the most promising NNMCs.[2−4] Although the exact nature of the active sites in NNMCs responsible for high ORR activity is not clearly understood, mass spectrometric evidence has revealed that catalysts with $Fe-N_{2+2}$ (with four pyridinic N, which are distinctive from the $Fe-N_4$ structure in the Fe-macrocycles having pyrrolic N[5]) possess higher ORR activity.[5−7] Using this understanding, researchers have developed highly active Fe−N−C catalysts,[4] rivaling state-of-the-art Pt/C, by choosing the right combination of starting C, Fe, N precursors and heat-treatment conditions. While these highly active Fe−N−C catalysts may reach the target activity for PEMFC commercialization, its chemical stability under the highly oxidizing environment of ORR for thousands of hours still remains a challenge.[4]

Carbon black (CB) is used typically to react with Fe and N precursors in the synthesis of $Fe-N-C_{CB}$ catalysts to host $Fe-N_x$ moieties. Fe-macrocycles such as Fe-phthalocyanine[8−10] and Fe-porphyrin,[11,12] having a $Fe-N_4$ moiety (Fe(III) with 4 pyrrolic N), have been first used to introduce Fe−N moieties into CB at elevated temperatures under inert gas atmosphere.[13−16] Subsequently, it is shown that the use of a Fe-macrocycle precursor is not required for incorporation, and NH_3 gas can be used to react with Fe salts such as Fe(II) acetate and Fe(III) chloride to form Fe−N moieties directly.[4,17−19] As micropores (less than 2 nm of pore sizes) in carbon are shown to correlate with the Fe−N−C site densities,[4,5] chemical treatments through carbon oxidation in acid[20,21] or carbon gasifications in NH_3[18,22−24] have been used to increase the densities of $Fe-N_x$ sites and thus the ORR activity. However, the carbon gasification can induce severe loss of carbon mass and consequently shorten the lifespan of these catalysts.[25] The instability of $Fe-N-C_{CB}$ prepared in NH_3 gas is apparent in the accelerated PEMFC testing, which shows ∼56% loss in the ORR activity at 0.5 V for 100 h in H_2/O_2 PEMFCs at 80 °C.[4] One strategy to improve the stability of these Fe−N−C catalysts is to increase the graphitization by pyrolyzing in inert gas.[25,26] However, such a method often reduces ORR activity, which likely results from micropore alternation and decreased active ORR site densities during pyrolysis.[25,26]

Here, we report the synthesis of a graphene-based Fe−N−C catalyst with high ORR activity and stability in acid. Graphene is a novel form of carbon, which has been explored recently in nanostructured electrodes for electrochemical capacitors,[27−29] ORR in alkaline fuel cells,[30] and biosensing[31] because of its very high surface area[27] and flexible surface functionalization chemistry.[32,33] In this study, we introduce Fe−N moieties into graphene (Fe−N−*r*GO) through the pyrolysis of chemically reduced-graphene oxide (*r*GO), Fe salt, and graphitic carbon nitride (g-C_3N_4). The surface chemical composition of Fe−N−*r*GO is examined by X-ray photoelectron spectroscopy (XPS) and the atomic coordination of Fe is studied by extended

Received: January 9, 2011
Revised: June 1, 2011
Published: July 18, 2011

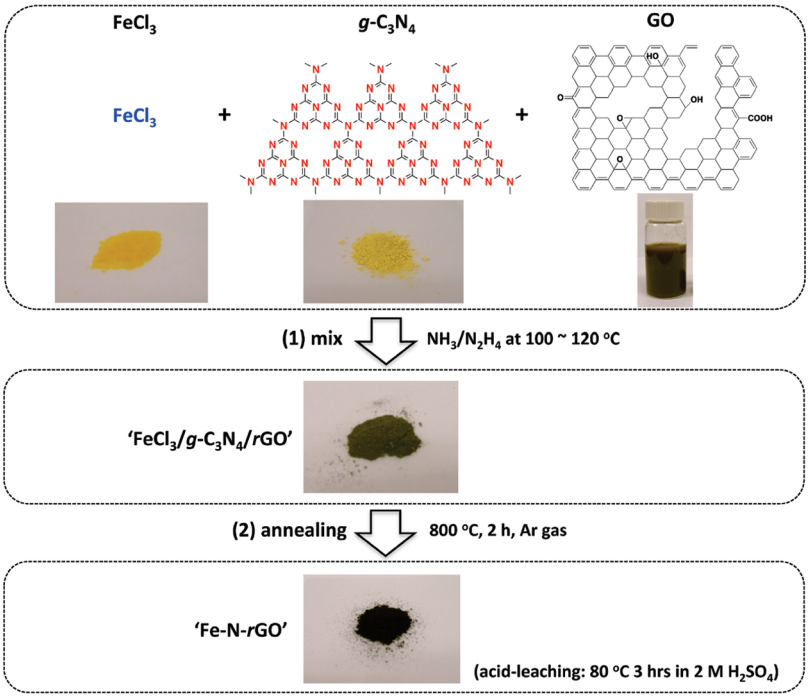

Figure 1. Schematic illustration of Fe−N−*r*GO synthesis and optical images of powder samples at various stages of synthesis.

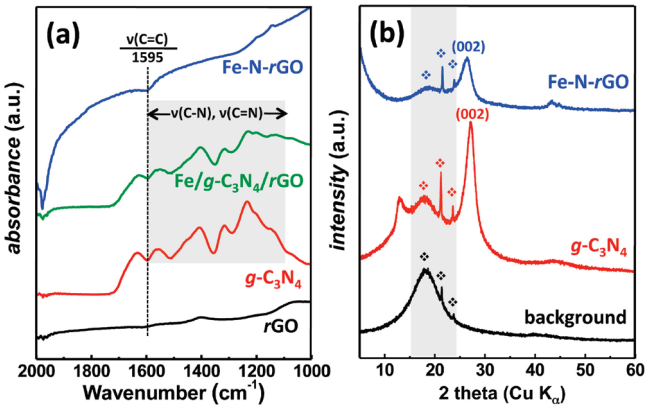

Figure 2. Characterization of powder samples. (a) ATR FT-IR of *r*GO (black), *g*-C_3N_4 (red), Fe/*g*-C_3N_4/*r*GO (green), and Fe−N−*r*GO (blue) (from bottom to top). The peaks in the gray box area are stretching vibration modes of C−N and C═N obtained from *g*-C_3N_4. (b) Powder XRD patterns of *g*-C_3N_4 (red), and Fe−N−*r*GO (blue).

X-ray absorption fine structure (EXAFS). The graphene-based catalyst shows higher ORR activity than CB-based catalysts synthesized by the same method, and it exhibits comparable activity but enhanced stability for ORR to the state-of-the-art CB-based catalysts reported previously.[2,4]

RESULTS AND DISCUSSION

The synthesis details of graphene-based catalyst samples are summarized in Figure 1. In the first step, *g*-C_3N_4 and $FeCl_3$ (6 wt %) were suspended in deionized (DI) water. Graphene oxide (GO) was added to the suspension and then reduced by adding a mixed NH_3/N_2H_4 solution at 80−100 °C. The resulting powder mixture ($FeCl_3$/*g*-C_3N_4/*r*GO) was collected after drying via vacuum filtration. The *g*-C_3N_4 precursor was polymerized thermally from dicyandiamide and employed as the N source.[34−37] The GO precursor was prepared by a modified Hummers method,[38,39] where oxygen-functional groups associated with GO such as hydroxyl and epoxide,[40] was reduced to *r*GO by NH_3/N_2H_4.[40,41] The $FeCl_3$/*g*-C_3N_4/*r*GO mixture showed a homogeneous dark green color that was derived from the yellowish $FeCl_3$ and *g*-C_3N_4 and the black *r*GO (Figure 1). In the second step (Fe/N impregnation), the $FeCl_3$/*g*-C_3N_4/*r*GO powder mixture was heated at 800 °C for 2 h under Ar. Upon annealing at 800 °C, the mass of the $FeCl_3$/*g*-C_3N_4/*r*GO mixture decreased by ∼80 wt.% (Figure S1 of the Supporting Information). The first mass loss of ∼15 wt % occurred in the temperature range of 200−300 °C, which resulted from removal of residual oxygen-containing groups on the *r*GO.[41] The second mass loss of ∼65 wt % in the temperature range from 620 to 700 °C came from the sublimation of *g*-C_3N_4.[36] This Fe/N impregnation was supported by the attenuated total reflectance (ATR) FT-IR and powder X-ray diffraction (XRD) (Figure 2).

Table 1. Surface Chemical Composition and Atomic Coordination Analysis of Fe−N−*r*GO. (a) Atomic Concentration of N, O, Fe, and Pyridinic N Relative to C Obtained by XPS. (b) EXAFS Analysis of Fe−N−*r*GO Fitted at Fe−N and Fe−Fe Scattering Positions

(a) XPS	atomic N/C	atomic O/C	atomic Fe/C	$N_{pyridinic}$/C
	0.052	0.037	0.004	0.021
(b) EXAFS	fraction	CN(x)[a]	R (Å)	
Fe−N	0.80	2.89 (±0.64)	1.89 (±0.05)	
Fe−Fe[b]	0.20	8 and 4	2.48 and 2.87[c]	

[a] Coordination number. [b] Two nearest coordinations for Fe−Fe were factored into account for first shell calculation. [c] The bond distances of Fe−Fe bonds were fixed during the fit.

dx.doi.org/10.1021/cm2000649 |*Chem. Mater.* 2011, 23, 3421–3428

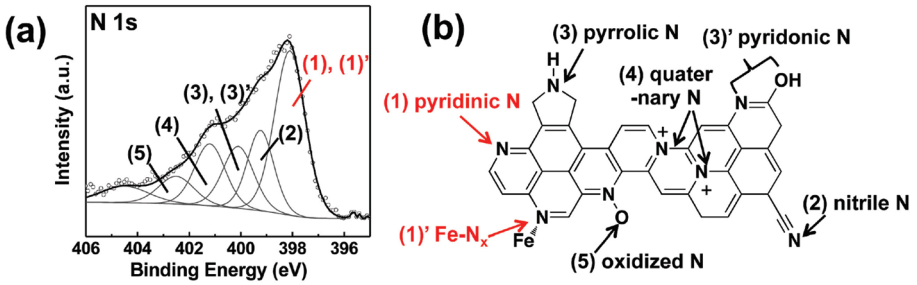

Figure 3. (a) XPS N 1s binding energy region of Fe−N−*r*GO sample. In the N 1s region, the numerical numbers indicate (1) pyridinic N and (1)′ Fe−N_x, (2) nitrile N, (3) pyrrolic N and (3)′ pyridonic N, (4) quaternary N, and (5) oxidized N. (b) Schematic of heterocyclic N structures.[44]

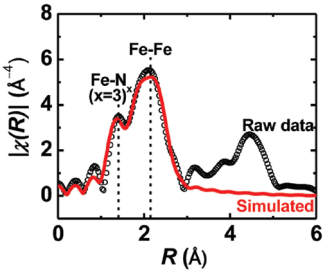

Figure 4. EXAFS raw data (black circles) and simulation (red line) curves of Fe−N−*r*GO.

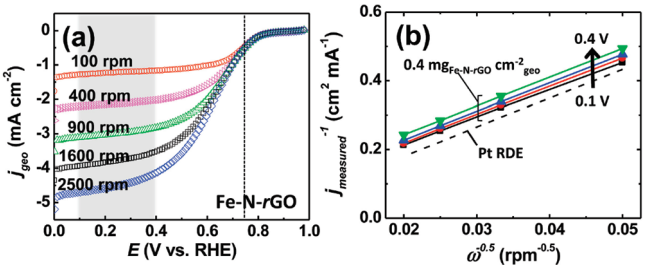

Figure 5. ORR activity of Fe−N−*r*GO in O_2-saturated 0.5 M H_2SO_4 at 10 mV s^{-1} and with a catalyst loading of 0.4 $mg_{Fe-N-rGO}$ cm^{-2}_{geo}. (a) Polarization curves of Fe−N−*r*GO from 100 to 2500 rpm of rotation rates. (b) Koutecky−Levich plots of Fe−N−*r*GO at a potential range of 0.1 to 0.4 V vs RHE from bottom to top. The dashed line represents the corresponding data for a polycrystalline Pt disk at 0.3 V vs RHE.

After pyrolysis, aromatic C−N and C═N stretching modes at the range of 1100−1600 cm^{-1} presented in the ATR FT-IR spectra for the *g*-C_3N_4 powder (red) and the $FeCl_3$/*g*-C_3N_4/*r*GO mixture (green),[34,42] disappeared while a skeletal stretching vibration peak of aromatic C═C rings near 1600 cm^{-1} became visible (blue in Figure 2a). XRD of the pyrolyzed powder showed that peaks at 13.1° (0.68 nm) and 27.4° (0.33 nm) of 2*theta, characteristic to *g*-C_3N_4 (red)[34−37] was replaced by a new peak at 26.2° (0.34 nm) of 2*theta, corresponding to the (002) stacking of graphitic carbon (blue in Figure 2b). The pyrolyzed product was acid-leached in 2 M H_2SO_4 at 80 °C for 3 h in order to remove extraneous Fe species such as iron oxide, and metallic iron.[14,43] The acid-treated, pyrolyzed sample was referred to as "Fe−N−*r*GO".

XPS and EXAFS of the Fe−N−*r*GO sample provided further evidence for the incorporation of Fe ion and N into the *r*GO upon annealing. Most of oxygen-containing functional groups derived from the GO (∼45 of O/C atomic concentration (atom %))[29] were removed after the NH_3/N_2H_4 reduction and subsequent annealing in Ar. As shown in part (a) of Table 1, the atomic ratios of N (N 1s in Figure 3a), O (O 1s in Figure S2 of the Supporting Information), and Fe (Fe 2p in Figure S2 of the Supporting Information) relative to C of the Fe−N−*r*GO sample were ∼0.052, 0.037, and 0.004, respectively. It should be noted that the signal of Fe (Fe 3p, 52−56 eV) was too weak to determine the Fe valence state. The XPS N 1s spectrum revealed the presence of (1) pyridinic N and (1)′ Fe−N_x (398 eV), (2) nitrile N (399 eV), (3) pyrrolic N and (3)′ pyridonic N (400 eV), (4) quaternary N (401 eV), and (5) oxidized N (402−405 eV) (Figure 3).[44,45] Note that pyridinic N has the highest concentration (40 atom %) among all N components (Figure 3 and Table S1 of the Supporting Information). Interestingly, this Fe−N−*r*GO sample, which might have acquired N from *r*GO (some N obtained from the hydrazine heat-treatment[29]) and/or *g*-C_3N_4 during pyrolysis, showed a higher fraction of pyridinic N than N-containing graphenes prepared by chemical vapor deposition growth with NH_3 gas,[30,46] and post-treatments of GO with either NH_3 gas annealing[47] or N_2 plasma,[31] all of which had shown predominantly quaternary N.

Because pyridinic N can coordinate with Fe,[4,5,7,48] our XPS finding pointed to the formation of Fe−N moieties into the graphene sheets, which was further supported by EXAFS analysis. The average coordination number (*x*) of Fe−N_x in the Fe−N−*r*GO sample was found to be 2.9 (±0.6) (Figure 4 and part (b) of Table 1), which was calculated using FEFFIT package (see Experimental Section and Supporting Information). The average bond length was 1.89 Å (±0.05), which was compressed relative to the square planar of Fe−N_4 (∼1.972 Å using iron(III) tetramethoxyphenylporphyrin (FeTMPP) model compound[49]). On the basis of the average coordination number, the Fe−N configurations in the Fe−N−*r*GO sample may be a combination of Fe−N_{2+2}, and/or its incomplete form (Fe−N_3), the former of which had been the proposed active Fe−N moieties for catalyzing the ORR.[5−7] On the basis of the high percentage of the pyridinic N species found in our XPS analysis, we caution that these proposed N coordinations of the catalytic sites may represent a catalytically different site from the Fe−N_4 group in macrocycles. In addition, EXAFS data revealed the presence of Fe metallic particles in the Fe−N−*r*GO sample as evidenced by the presence of the Fe−Fe scattering (Figure 4 and part (b) of Table 1), which was confirmed by transmission electron microscope (TEM) imaging in Figure S3 of the Supporting Information. The presence of Fe nanoparticles (NPs) is commonly noted during annealing[50] or reduction of Fe salt precursor by N_2H_4.[51]

The ORR activity of Fe−N−*r*GO was investigated by using a thin-film rotating disk electrode (RDE) in O_2-saturated 0.5 M

dx.doi.org/10.1021/cm2000649 |*Chem. Mater.* 2011, 23, 3421–3428

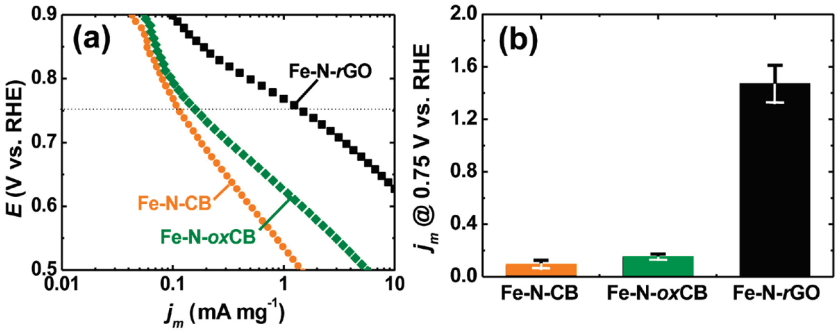

Figure 6. Comparison of ORR mass activity from RDE measurements. (a) Tafel plots of Fe−N−CB (orange), Fe−N−*ox*CB (green), and Fe−N−*r*GO (black) in O_2-saturated 0.5 M H_2SO_4 at 10 mV s^{-1} of scan rate and 900 rpm of rotation rate (0.4 $mg_{Fe-N-CB}$ cm^{-2}_{geo}), which were corrected for capacitive currents and mass transport. (b) ORR mass activity of Fe−N−CB (orange), Fe−N−*ox*CB (green), and Fe−N−*r*GO (black) at 0.75 V vs RHE extracted from (a). Error bars indicating standard deviations from averaged values at 0.75 V vs RHE of two Fe−N−CB, two Fe−N−*ox*CB, and four Fe−N−*r*GO samples.

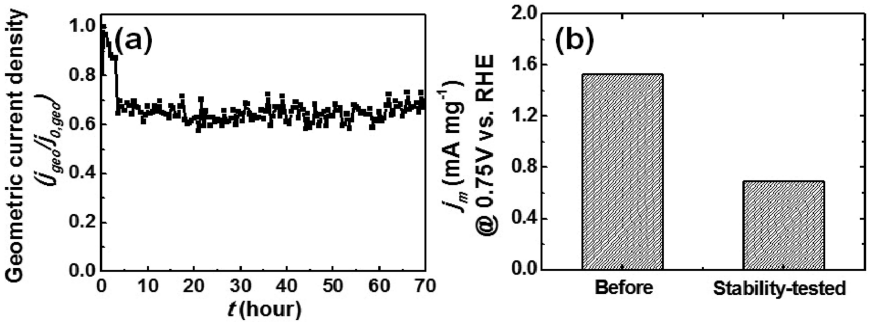

Figure 7. Durability of Fe−N−*r*GO. (a) Chronoamperometry of Fe−N−*r*GO in O_2-bubbled 0.5 M H_2SO_4 at 80 °C for 70 h. The potential was held at 0.5 V vs RHE. (b) Decreased ORR activity of Fe−N−*r*GO before and after 24 h of stability test measured at 0.75 V vs RHE, room temperature, 10 mV s^{-1} of scan rate, and 900 rpm of rotation rate (0.4 $mg_{Fe-N-rGO}$ cm^{-2}_{geo}). The mass activities of before and after stability tests are 1.5 and 0.7 mA $mg^{-1}_{Fe-N-rGO}$, respectively.

H_2SO_4 at a scan rate of 10 mV s^{-1}. The Fe−N−*r*GO catalyst (0.4 $mg_{Fe-N-rGO}$ cm^{-2}_{geo}) had a mass activity of 0.5 and 1.5 mA $mg^{-1}_{Fe-N-rGO}$ at 0.80 and 0.75 V vs RHE (Figure 5a), respectively. Diffusion-limited current densities collected at different rotation rates in the potential range from 0.1 to 0.4 V vs RHE (gray area in Figure 5a) were used to determine to the number of electrons transferred associated with ORR, which was calculated to be ~4 by the Koutecky−Levich equation (Figure 5b). This result was in good agreement with that (~3.7) as determined from the H_2O_2 molar fraction relative to H_2O obtained from rotating ring disk electrode (RRDE) measurements.

Increasing the annealing temperature beyond 700 °C did not lead to substantial increases in the ORR mass activity at 0.75 V vs RHE (Figure S4a of the Supporting Information), but a significant increase in the activity of catalysts heat-treated between 600 and 700 °C was observed. We attribute this large ORR activity increase to the integration of Fe−N_x moieties in *r*GO sheets, which is presumably associated with the sublimation and pyrolysis of *g*-C_3N_4 at temperatures above 600 °C (Figures S4a and S1 of the Supporting Information). In addition, varying the concentration of Fe precursor ($FeCl_3 \cdot 6H_2O$) in the range of 1 to 6 wt % did not lead to ORR activity enhancement (Figure S4b of the Supporting Information).

As a baseline comparison, the ORR activity of Fe−N−*r*GO was compared with the Fe−N−C catalysts prepared using commercial CB (Vulcan XC-72, Cabot) and oxidized CB (*ox*CB).[20] Fe−N−C catalysts made from CB and *ox*CB (Fe−N−CB and Fe−N-*ox*CB) were synthesized from $FeCl_3$/*g*-C_3N_4/CB and $FeCl_3$/*g*-C_3N_4/*ox*CB using the same method shown in Figure 1, respectively. As shown in Figure 6, the Fe−N−*r*GO had significantly higher ORR mass activity than the either Fe−N−CB or Fe−N-*ox*CB catalysts (roughly by 1 order of magnitude), which suggests that N-doped carbon species derived from *g*-C_3N_4 if formed during pyrolysis are not primarily responsible for the high ORR activity observed for Fe−N−*r*GO. It should be noted that Fe−N−CB and Fe−N−*ox*CB catalysts prepared in this study showed much lower ORR mass activity of previously reported Fe−N−CB catalysts synthesized by different methods.[26,45,50] The enhanced ORR mass activity of Fe−N−*r*GO relative to Fe−N−CB and Fe−N−*ox*CB might be attributed to the fact that carbon atoms in the *r*GO matrix can potentially provide unique carbon chemistry,[52] which may facilitate the formation of Fe−N_x[4] and N[53] groups (proposed as active sites for ORR) using the synthesis method employed in this study. As the Raman,[3,54,55] XRD,[56,57] and high-resolution TEM[50,58] data of CB and *r*GO are similar, it is not straightforward to reveal the atomic structure differences between *r*GO and CB and how they changed during the catalyst synthesis using conventional characterization tools. Future studies including aberration-corrected scanning transmission electron microscopy at low voltages such as 60 keV would be very helpful to examine the structure and chemistry of these catalysts on the atomic scale.

dx.doi.org/10.1021/cm2000649 |*Chem. Mater.* 2011, 23, 3421–3428

The ORR mass activity of Fe−N−*r*GO in this study (~0.5 and ~1.5 mA $mg^{-1}_{Fe-N-rGO}$ at 0.8 and 0.75 V vs RHE, respectively) is within a factor of 3 of the highest ORR activity reported for Fe−N−C catalysts[26,45,50] synthesized from Fe salt-based precursor in inert atmosphere (1.3 mA mg^{-1} for FeCo−PANI−C at 0.8 V vs RHE[50]). As the ORR mass activity of the NNMCs from RDE measurements can differ from those obtained from PEMFC tests,[45] only the ORR mass activity of NNMCs obtained from RDE measurements reported previously[26,45,50] is compared in this study. Notably, the Fe−N−*r*GO has lower ORR mass activity than the Fe−N−C_{CB} samples made in reactive atmosphere such as NH_3 gas (~5.0 mA mg^{-1}_{Fe-N-C} at 0.8 V vs RHE),[45,59] which can be attributed to higher yield of pores and active sites in the carbon particles than that in inert atmosphere.[18] However, the high activity of Fe−N−C_{CB} obtained by NH_3 gas annealing degrades quickly over time as shown by previous studies.[4,25] In comparison to previous Fe−N−C_{CB} catalysts obtained from NH_3 annealing, the Fe−N−*r*GO catalyst in this study showed moderately higher stability for ORR, which is discussed in the following.

The stability of Fe−N−*r*GO for ORR was studied by examining how the ORR current changed as a function of time at 0.5 V vs RHE. The ORR current of Fe−N−*r*GO remained constant over 70 h at 0.5 V vs RHE in O_2-bubbled 0.5 M H_2SO_4 at 80 °C (Figure 7a) despite a initial drop of 30% in the first 3 h. Considering the electrochemical active surface area of Fe−N−*r*GO is nearly unchanged as evidenced by comparable electrochemical capacitance and redox peak intensities before and after the stability test (Figure S5 of the Supporting Information), it is proposed that the ORR activity reduction can be attributed to loss of active sites for ORR. The stability of Fe−N−*r*GO was compared with that of previously reported Fe−N−C_{CB} catalysts[4,25] with comparable or higher ORR activity but not with low-activity Fe−N−CB and Fe−N−*ox*CB catalysts synthesized in this study. Fe−N−*r*GO was found to have higher stability than Fe−N−C_{CB} synthesized in NH_3 (~50% loss of current density at 0.5 V for 70 h in H_2/O_2 PEMFCs at 80 °C[4]). It is hypothesized that the enhanced stability of Fe−N−*r*GO for ORR can be attributed to (1) higher degree of graphitization[25] of Fe−N−*r*GO relative to Fe−N−C_{CB} catalysts prepared in NH_3, and/or (2) reduced H_2O_2 production during ORR. Specifically, hydroxyl radicals could severely attack active sites,[25] which is supported by the observation that H_2O_2 treatment has led to (1) a decrease in the ORR activity of Fe−N−C_{CB} catalyst more than acid treatment,[15] (2) a decrease of Fe and N densities,[26] and (3) a change of heterocyclic N structures.[26]

RRDE measurements of Fe−N−*r*GO were used to quantify the amount of H_2O_2 generation during ORR. H_2O_2 can be generated via 2e-transfer ORR ($O_2 + 2H^+ + 2e^- \rightarrow H_2O_2$), where it can be further reduced to H_2O via either electroreduction ($H_2O_2 + 2H^+ + 2e^- \rightarrow 2H_2O$) or disproportionation ($H_2O_2 \rightarrow H_2O + 1/2O_2$). The higher loading of catalysts used for RRDE measurements, the less likely H_2O_2 produced being detected by RRDE measurements, as shown previously.[60,61] This trend was also found in this study, where the amount of H_2O_2 detected was decreased with increasing Fe−N−*r*GO loading on glassy carbon (GC) from 0.8 to 0.04 $mg_{Fe-N-rGO}$ cm^{-2}_{geo} (Figures S6, S7 of the Supporting Information). It is worth noting that the GC substrate plays a negligible role in the H_2O_2 production (Figure S6 of the Supporting Information). Therefore, we focus on the result obtained from the low loading, which most accurately reflects the intrinsic amount of H_2O_2 produced during ORR. Interestingly, the ORR on the Fe−N−*r*GO sample was shown to have ~3.4 electrons transferred during ORR and produce less H_2O_2 (~30% H_2O_2 in 0.04 $mg_{Fe-N-rGO}$ cm^{-2}_{geo} at 900 rpm) than previously reported Fe−N−C_{CB}[60] (~80% H_2O_2 with a comparable loading of 0.04 mg $_{Fe-N-C}$ cm^{-2}_{geo} at 900 rpm shown in Figure S7 of the Supporting Information). It should be mentioned that the Fe−N−*r*GO sample does not produce the least amount of H_2O_2 production in comparison to the latest Fe−N−C_{CB} catalysts reported (ours is ~20% at 0.08 $mg_{Fe-N-rGO}$ cm^{-2}_{geo} vs ~10% at 0.1 mg cm^{-2}_{geo} reported previously,[61] where the durability of the catalysts is not known). Although other parameters cannot be excluded, reduced H_2O_2 production is a likely contributor for the enhanced ORR stability of Fe−N−*r*GO relative to some highly active Fe−N−C_{CB} catalysts.

Although the stability of NNMC catalysts is often compared at 0.5 V vs RHE in the literature,[4,50] current densities near this voltage are limited largely by the diffusion of O_2 but not the ORR kinetics. To reveal the degradation of the intrinsic ORR activity near the kinetic region, we also measured the ORR activity of Fe−N−*r*GO at 0.75 V vs RHE, room temperature, and 900 rpm of rotation rate after 24 h of the stability test. The ORR activity was found to decrease to ~45% of the original value (Figure 7b), and the reduction is more severe than that shown in panel (a) of Figure 7, which highlights the need of future studies to measure and compare the stability of NNMCs for ORR in the voltage region having ORR kinetic limiting.

CONCLUSIONS

We have successfully made a graphene-based catalyst and have studied its catalytic functionality to promote the ORR kinetics in acid. EXAFS analysis shows that the graphene-based catalyst has an Fe−$N_{3,average}$ moiety, while XPS measurements reveals that the catalyst surface consists of ~5 atom % N (largely pyridinic-like) and ~0.4 atom % Fe relative to C (the signal too weak to reveal the valence state of Fe). This graphene-based catalyst exhibits ORR mass activity approaching those of the state-of-the-art NNMCs reported to date, which highlights the opportunities of utilizing unique surface chemistry of *r*GO to create active Fe−N_x sites and develop highly active NNMCs.

EXPERIMENTAL SECTION

Synthesis of Fe−N−*r*GO. A GO solution was made using a modified Hummers method.[38−40] Further details can be found in the Supporting Information. A *g*-C_3N_4 powder sample was synthesized by thermal polymerization of dicyandiamide (Sigma-Aldrich).[36] Using a gas tube furnace, 3 g of dicyandiamide powder was heat-treated at 550 °C for 4−5 h with 2.3 °C min^{-1} of ramping rate and ~20 cc min^{-1} of Ar gas flow. The yellow *g*-C_3N_4 powder was ground using mortar and pestle. For the preparation of typical Fe−N−*r*GO, 0.25 g of *g*-C_3N_4 and 0.025 g of $FeCl_3 \cdot 6H_2O$ (Sigma-Aldrich) were put in DI water. After heating up to 80 °C with vigorous stirring, 100 mL of GO solution (1.25 mg mL^{-1}) was added, which was collected from sonication (100 W for 1 h) and centrifugation (3000 rpm for 1 h). Then the reducing reagents (350 μL of NH_3, 28 w/w in water, Alfa Aesar and 50 μL of N_2H_4 (hydrazine) solutions, 35 wt % in water, Sigma-Aldrich) were sequentially inserted at 100 °C. The mixture was vigorously stirred at 130 °C in order to prevent an inhomogeneous mixing until the aqueous solution was

completely evaporated and then collected and ground using the mortar and pestle. This powder mixture ($FeCl_3$/*g*-C_3N_4/*r*GO) in a ceramic crucible was transferred to the gas tube furnace. The temperature of tube furnace was elevated to 800 at 100 °C min^{-1} of ramping rate and ~20 cc min^{-1} of Ar gas flow and held at 800 °C for 2 h, which was then cooled to room temperature. The sample was acid-leached in 2 M H_2SO_4 at 80 °C for 3 h before characterization, which was referred to as "Fe−N−*r*GO".

To make Fe−N−CB and Fe−N−*ox*CB, 0.025 g of $FeCl_3 \cdot 6H_2O$, 0.25 g of *g*-C_3N_4, and 0.125 g of Vulcan XC-72 were mixed. The *ox*CB was prepared by (1) washing of Vulcan XC-72 in 37% of HCl (Aldrich) overnight, (2) refluxing in HNO_3 at 70 °C for 2 h, and then (3) thoroughly washing in DI water and drying in oven.[20] All pyrolysis processes were identical with the steps described for Fe−N−*r*GO.

Characterization. Identification of the chemical functional groups of the powder samples was conducted using ATR FT-IR (Nexus). Surface morphologies of Fe−N−*r*GO were investigated using SEM (JEOL JSM-6060) and TEM (JEOL 2010). The TGA Q50 (TA Instruments) under N_2 gas flow (90 mL min^{-1}) was conducted with a heating window of 50 to 800 at 10 °C min^{-1} of ramping rate. The XPS data was obtained by Kratos AXIS ultra imaging XPS using monochromatic Al anode. All spectra were calibrated by setting the C 1s photoemission peak for sp^2-hybridized carbons to 284.5 eV and were fitted after a Shirley type background subtraction. The XRD patterns were collected using Rigaku H3R Cu-source 185 mm goniometer (Cu Kα = 1.5218 Å) with a 0.5° of divergence slit, 0.5° of scatter slit, 0.3 mm of receiving slit, and 0.8 mm of monochromator receiving slit. A scan rate of 1 deg min^{-1} was used, and a 2*theta range from 5 to 60 degrees was scanned.

EXAFS Analysis. *X*-ray absorption spectroscopy (XAS) was conducted at beamline X11A of the National Synchrotron Light Source at the Brookhaven National Laboratory (BNL). The Fe K-edge fluorescence mode was collected using Lytle detector using Si(111) double-crystal monochromator detuned to ~60% of the maximum intensity. EXAFS spectrum was extracted from the absorbance by subtracting from the pre-edge region using a linear fit and normalizing the postedge region using a cubic spline fit. Fourier transform to *R*-space was applied to 2−10 $Å^{-1}$ region using a Hanning window of 1 $Å^{-1}$. All of the theoretical variables for EXAFS paths (Fe−N and Fe−Fe) were calculated using FEFF 6 software,[62] and were refined by fitting the previously reported crystal structures to the FeTMPP (square planar of $Fe-N_4$)[63] reference compound for Fe−N and Fe foil for Fe−Fe using IFEFFIT package. The first shell of the scattering was fitted by assuming the presence of only Fe−N and Fe−Fe paths, where the scattering characteristics (the passive electron reduction values, mean square displacement, etc.) were assumed to be the same as the reference molecules of FeTMPP-Cl and Fe foil, respectively. Further details can be found in the Supporting Information.

RDE Measurements of ORR Activity and Stability. Sixteen milligrams of Fe−N−*r*GO powder was dispersed in mixture of 1500 μL of DI water, 420 μL of ethanol, and 80 μL of Nafion (5 wt % solution in a mixture of lower aliphatic alcohols and water, Aldrich). The ink solution, kept in a sealed vial, was sonicated (100W for 1 h) and stirred at least 5 days. Ten microliters aliquot of catalyst ink was dropped on a GC (0.196 cm^2 of geometric area (*geo*), Pine Research Instrument) and was dried at room temperature overnight. On the basis of the ink composition, a total catalyst loading mass on the GC electrode was ~80 $\mu g_{Fe-N-rGO}$, which corresponded to a loading amount of 0.4 mg $_{Fe-N-rGO}$ $cm^{-2}{}_{geo}$ on the basis of the geometric area of GC. The drop-cast catalyst on the GC was mounted to a rotator of bipotentiostat (Pine Research Instruments) and used as the working electrode with a Pt wire as the counter and a saturated calomel electrode (SCE, Analytical Sensor, Inc.) as the reference. Polarization curves were collected using the RDE technique by scanning from −0.25 to +0.75 V vs SCE in O_2-saturated 0.5 M of H_2SO_4 at 10 mV s^{-1} scan rate and 100−2500 rpm of rotation rates. The backward and forward scans were averaged to remove the capacitive current contribution (Figure S8 of the Supporting Information), were subsequently mass transport corrected (considering a diffusion-limited current density for 0.4 $mg_{catalyst}$ $cm^{-2}{}_{geo}$, of 3.1 mA $cm^{-2}{}_{geo}$ at 900 rpm, corresponding to a limited current of ≈3.7 electrons transferred), and were applied to obtain the ORR kinetic current,[64] which was normalized to mass loading to yield ORR mass activity in mA $mg^{-1}{}_{catalyst}$. The analysis of the number of electrons transferred during ORR from the diffusion-limited currents can be found in the Supporting Information. Chronoamperometries of a Fe−N−*r*GO electrode (0.4 mg $_{Fe-N-rGO}$ $cm^{-2}{}_{geo}$) were examined in O_2-bubbled 0.5 M H_2SO_4 at 80 °C for 70 h, where the potential was held at 0.5 V vs RHE. All the electrochemical results reported in this work referred to the reversible hydrogen electrode (RHE) as calibrated at the reversible potential of the hydrogen oxidation reaction on polycrystalline Pt disk (Pt-RDE) in H_2-saturated 0.5 M H_2SO_4 at a scan rate of 10 mV s^{-1} and 900 rpm per each experimental set, which was +0.250 ± 0.002 V vs SCE to convert the value vs RHE in general.

RRDE Measurements of H_2O_2 Production during ORR. The RRDE collection efficiency was calibrated using forward scans of disk (I_d) and Pt ring currents (I_r) at 20 mV s^{-1} of the scan rate in 0.1 M NaOH with a 10 mM $K_3Fe(CN)_6$ (99+%, Sigma-Aldrich) electrolyte.[65] The disk potential was swept from −0.55 to 0.45 V vs SCE, while the Pt ring potential was held at 0.45 V vs SCE. The collection efficiency (N) was determined from eq 1.[65]

$$N = \frac{I_r}{|I_d|} \tag{1}$$

The estimated ring collection efficiency was 0.21 ± 0.004 in our system. The fraction of H_2O_2 generated from the ORR was measured by scanning the catalyst-loaded disk from −0.25 to +0.75 V vs SCE at 10 mV s^{-1} of the scan rate while holding the Pt ring at +1.10 V vs SCE in O_2-saturated 0.5 M H_2SO_4.[65] The measured I_r was corrected by subtracting the background currents. The percentage of H_2O_2 was estimated from eq 2.[65]

$$H_2O_2(\%) = \frac{2 \times I_r}{(N \times |I_d|) + I_r} \times 100 \tag{2}$$

The number of electrons transferred (n) was estimated from eq 3 using the H_2O_2 molar fraction.[65]

$$n = 4 - \left(2 \times \frac{H_2O_2\ (\%)}{100}\right) \tag{3}$$

The Fe−N−*r*GO catalyst loading was varied from 0.04−0.8 $mg_{Fe-N-rGO}$ $cm^{-2}{}_{geo}$.

■ ASSOCIATED CONTENT

Supporting Information. Details of experimental section, TGA graph, XPS analysis, SEM, TEM images, a comparison of ORR activities with respect to an annealing temperature and

concentration, and $\%H_2O_2$ curves. This material is available free of charge *via* the Internet at http://pubs.acs.org.

AUTHOR INFORMATION

Corresponding Author

*E-mail: shaohorn@mit.edu.

Present Addresses

[||]RIKEN Advanced Science Institute, 2-1 Hirosawa, Wako, Saitama 351-0198 Japan.

ACKNOWLEDGMENT

The authors thank Ethan J. Crumlin for collecting XPS data, Dr. Christopher Earl Carlton for taking TEM images, and Dr. Azzam N. Mansour for his assistance in the EXAFS data analysis. This work made use of the Shared Experimental Facilities supported by the MRSEC Program of the National Science Foundation under award DMR-0819762. Y.S.H. acknowledges the financial support of Eni S.p.A under the Eni-MIT Alliance Solar Frontiers. The National Synchrotron Light Source for EXAFS is supported by the U.S. Department of Energy, Division of Material Sciences and Division of Chemical Sciences, under contract DE-AC02-98CH10886. The beamline X11 is supported by the Office of Naval Research and contributions from Participating Research Team (PRT) members.

REFERENCES

(1) Gasteiger, H. A.; Kocha, S. S.; Sompalli, B.; Wagner, F. T. *Appl. Catal., B* **2005**, *56*, 9–35.

(2) Bashyam, R.; Zelenay, P. *Nature* **2006**, *443*, 63–66.

(3) Yuan, X.; Zeng, X.; Zhang, H. J.; Ma, Z. F.; Wang, C. Y. *J. Am. Chem. Soc.* **2010**, *132*, 1754–1755.

(4) Lefèvre, M.; Proietti, E.; Jaouen, F.; Dodelet, J. P. *Science* **2009**, *324*, 71–74.

(5) Charreteur, F.; Jaouen, F.; Ruggeri, S.; Dodelet, J. P. *Electrochim. Acta* **2008**, *53*, 2925–2938.

(6) Lefèvre, M.; Dodelet, J. P.; Bertrand, P. *J. Phys. Chem. B* **2000**, *104*, 11238–11247.

(7) Lefèvre, M.; Dodelet, J. P.; Bertrand, P. *J. Phys. Chem. B* **2002**, *106*, 8705–8713.

(8) van Veen, J. A. R.; Visser, C. *Electrochim. Acta* **1979**, *24*, 921–928.

(9) van Veen, J. A. R.; Colijn, H. A.; Visser, C. *Electrochim. Acta* **1988**, *33*, 801–804.

(10) Biloul, A.; Contamin, O.; Scarbeck, G.; Savy, M.; vanden Ham, D.; Riga, J.; Verbist, J. J. *J. Electroanal. Chem.* **1992**, *335*, 163–186.

(11) Gojković, S. Lj.; Gupta, S.; Savinell, R. F. *J. Electrochem. Soc.* **1998**, *145*, 3493–3499.

(12) Gojković, S. Lj.; Gupta, S.; Savinell, R. F. *J. Electroanal. Chem.* **1998**, *462*, 63–72.

(13) Bae, I. T.; Tryk, D. A.; Scherson, D. A. *J. Phys. Chem. B* **1998**, *102*, 4114–4117.

(14) Bouwkamp-Wijnoltz, A. L.; Visscher, W.; van Veen, J. A. R.; Boellaard, E.; van der Kraan, A. M.; Tang, S. C. *J. Phys. Chem. B* **2002**, *106*, 12993–13001.

(15) Schulenburg, H.; Stankov, S.; Schünemann, V.; Radnik, J.; Dorbandt, I.; Fiechter, S.; Bogdanoff, P.; Tributsch, H. *J. Phys. Chem. B* **2003**, *107*, 9034–9041.

(16) Koslowski, U. I.; Abs-Wurmbach, I.; Fiechter, S.; Bogdanoff, P. *J. Phys. Chem. C* **2008**, *112*, 15356–15366.

(17) Faubert, G.; Côté, R.; Dodelet, J. P.; Lefèvre, M.; Bertrand, P. *Electrochim. Acta* **1999**, *44*, 2589–2603.

(18) Jaouen, F.; Lefèvre, M.; Dodelet, J. P.; Cai, M. *J. Phys. Chem. B* **2006**, *110*, 5553–5558.

(19) Jaouen, F.; Charreteur, F.; Dodelet, J. P. *J. Electrochem. Soc.* **2006**, *153*, A689–A698.

(20) Nallathambi, V.; Lee, J. W.; Kumaraguru, S. P.; Wu, G.; Popov, B. N. *J. Power Sources* **2008**, *183*, 34–42.

(21) Schilling, T.; Bron, M. *Electrochim. Acta* **2008**, *53*, 5379–5385.

(22) Lefèvre, M.; Dodelet, J. P. *Electrochim. Acta* **2008**, *53*, 8269–8276.

(23) Médard, C.; Lefèvre, M.; Dodelet, J. P.; Jaouen, F.; Lindbergh, G. *Electrochim. Acta* **2006**, *51*, 3202–3213.

(24) Ruggeri, S.; Dodelet, J. P. *J. Electrochem. Soc.* **2007**, *154*, B761–B769.

(25) Charreteur, F.; Jaouen, F.; Dodelet, J. P. *Electrochim. Acta* **2009**, *54*, 6622–6630.

(26) Wu, G.; Artyushkova, K.; Ferrandon, M.; Kropf, J.; Myers, D.; Zelenay, P. *ECS Trans.* **2009**, *1*, 1299–1311.

(27) Stoller, M. D.; Park, S.; Zhu, Y.; An, J.; Ruoff, R. S. *Nano Lett.* **2008**, *8*, 3498–3502.

(28) Zhu, Y.; Stoller, M. D.; Cai, W.; Velamakanni, A.; Piner, R. D.; Chen, D.; Ruoff, R. S. *ACS Nano* **2010**, *4*, 1227–1233.

(29) Byon, H. R.; Lee, S. W.; Chen, S.; Hammond, P. T.; Shao-Horn, Y. *Carbon* **2011**, *49*, 457–467.

(30) Qu, L.; Liu, Y.; Baek, J. B.; Dai, L. *ACS Nano* **2010**, *4*, 1321–1326.

(31) Wang, Y.; Shao, Y.; Matson, D. W.; Li, J.; Lin, Y. *ACS Nano* **2010**, *4*, 1790–1798.

(32) Dikin, D. A.; Stankovich, S.; Zimney, E. J.; Piner, R. D.; Dommett, G. H. B.; Evmenenko, G.; Nguyen, S. T.; Ruoff, R. S. *Nature* **2007**, *448*, 457–460.

(33) Stankovich, S.; Piner, R. D.; Chen, X.; Wu, N.; Nguyen, S. T.; Ruoff, R. S. *J. Mater. Chem.* **2006**, *16*, 155–158.

(34) Groenwolt, M.; Antonietti, M. *Adv. Mater.* **2005**, *17*, 1789–1792.

(35) Goettmann, F.; Fischer, A.; Antonietti, M.; Thomas, A. *Angew. Chem., Int. Ed.* **2006**, *45*, 4467–4471.

(36) Thomas, A.; Fischer, A.; Goettmann, F.; Antonietti, M.; Müller, J. O.; Schlögl, R.; Carlsson, J. M. *J. Mater. Chem.* **2008**, *18*, 4893–4908.

(37) Wang, X.; Chen, X.; Thomas, A.; Fu, X.; Antonietti, M. *Adv. Mater.* **2009**, *21*, 1609–1612.

(38) Hummers, W. S.; Offeman, R. E. *J. Am. Chem. Soc.* **1958**, *80*, 1339.

(39) Kovtyukhova, N. I.; Ollivier, P. J.; Martin, B. R.; Mallouk, T. E.; Chizhik, S. A.; Buzaneva, E. V.; Gorchinskiy, A. D. *Chem. Mater.* **1999**, *11*, 771–778.

(40) Li, D.; Müller, M .B.; Gilje, S.; Kaner, R. B.; Wallace, G. G. *Nature Nanotechnol.* **2008**, *3*, 101–105.

(41) Stankovich, S.; Dikin, D. A.; Piner, R. D.; Kohlhaas, K. A.; Kleinhammes, A.; Jia, Y.; Wu, Y.; Nguyen, S. B. T.; Ruoff, R. S. *Carbon* **2007**, *45*, 1558–1565.

(42) Zhao, Y. C.; Yu, D. L.; Zhou, H. W.; Tian, Y. J. *J. Mater. Sci.* **2005**, *40*, 2645–2647.

(43) Tributsch, H.; Koslowski, U. I.; Dorbandt, I. *Electrochim. Acta* **2008**, *53*, 2198–2209.

(44) Jurewicz, K.; Babeł, K.; Źiółkowski, A.; Wachowska, H. *Electrochim. Acta* **2003**, *48*, 1491–1498.

(45) Jaouen, F.; Herranz, J.; Lefère, M.; Dodelet, J. P.; Kramm, U. I.; Herrmann, I.; Bogdanoff, P.; Maruyama, J.; Nagaoka, T.; Garsuch, A.; Dahn, J. R.; Olson, T.; Pylypenko, S.; Atanassov, P.; Ustinov, E. A. *ACS Appl. Mater. Interfaces* **2009**, *1*, 1623–1639.

(46) Wei, D.; Liu, Y.; Wang, Y.; Zhang, H.; Huang, L.; Yu, G. *Nano Lett.* **2009**, *9*, 1752–1758.

(47) Li, X.; Wang, H.; Robinson, J. T.; Sanchez, H.; Diankov, G.; Dai, H. *J. Am. Chem. Soc.* **2009**, *131*, 15939–15944.

(48) Herranz, J.; Jaouen, F.; Dodelet, J. P. *ECS Trans.* **2009**, *25*, 117–125.

(49) Collman, J. P.; Hoard, J. L.; Kim, N.; Lang, G.; Reed, C. A. *J. Am. Chem. Soc.* **1975**, *97*, 2676–2681.

(50) Wu, G.; Chen, Z.; Artyushkova, K.; Garzon, F. H.; Zelenay, P. *ECS Trans.* **2008**, *16*, 159–170.

(51) Yang, C.; Xing, J.; Guan, Y.; Liu, J.; Liu, H. *J. Alloys Compd.* **2004**, *385*, 283–287.

(52) Paredes, J. I.; Villar-Rodil, S.; Solís-Fernández, P.; Martínez-Alonso, A.; Tascón, J. M. D. *Langmuir* **2009**, *25*, 5957–5968.
(53) Matter, P. H.; Ozkan, U. S. *Catal. Lett.* **2006**, *109*, 115–123.
(54) Jawhari, T.; Roid, A.; Casado, J. *Carbon* **1995**, *33*, 1561–1565.
(55) Gómez-Navarro, C.; Weitz, R. T.; Bittner, A. M.; Scolari, M.; Mews, A.; Burghard, M.; Kern, K. *Nano Lett.* **2007**, *7*, 3499–3503.
(56) Park, S.; An, J.; Potts, J. R.; Velamakanni, A.; Murali, S.; Ruoff, R. S. *Carbon* **2011**, *49*, 3019–3023.
(57) Beak, S.; Jung, D.; Nahm, K. S.; Kim, P. *Catal. Lett.* **2010**, *134*, 288–294.
(58) Ferreira, P. J.; la O, G. J.; Morgan, D.; Makharia, R.; Kocha, S.; Gasteiger, H. A. *J. Electrochem. Soc.* **2005**, *152*, A2256–A2271.
(59) Jaouen, F.; Proietti, E.; Lefèvre, M.; Chenitz, R.; Dodelet, J. P.; Wu, G.; Chung, H. T.; Johnston, C. M.; Zelenay, P. *Energy Environ. Sci.* **2011**, *4*, 114–130.
(60) Bonakdarpour, A.; Lefevre, M.; Yang, R.; Jaouen, F.; Dahn, T.; Dodelet, J. P.; Dahn, J. R. *Electrochem. Solid-State Lett.* **2008**, *11*, B105–B108.
(61) Jaouen, F.; Dodelet, J. P. *J. Phys. Chem. C* **2009**, *113*, 15422–15432.
(62) Rehr, J. J.; Albers, P. C. *Rev. Mod. Phys.* **2000**, *72*, 621–654.
(63) Scheidt, W. R.; Finnegan, M. G. *Acta Crystallogr.* **1989**, *C45*, 1214–1216.
(64) Suntivich, J.; Gasteiger, H. A.; Yabuuchi, N.; Shao-Horn, Y. *J. Electrochem. Soc.* **2010**, *157*, B1263–B1268.
(65) Paulus, U. A.; Schmidt, T. J.; Gasteiger, H. A.; Behm, R. J. *J. Electroanal. Chem.* **2001**, *495*, 134–145.